Improved photocatalytic removal of acid red 14 by amino-functionalized Fe$_3$O$_4$–WO$_3$ nanoparticles from aqueous solutions in the presence of UV irradiation

Azita Mohagheghian[a], Kobra Ayagh[a], Kazem Godini[b], Mehdi Shirzad-Siboni[a,c,d,*]

[a]*Department of Environmental Health Engineering, School of Health, Guilan University of Medical Sciences, Rasht, Iran,*
Tel. +98 9111309440; email: mohagheghian@yahoo.com (A. Mohagheghian), Tel. +98 9117217955;
email: kobra.ayagh89@yahoo.com (K. Ayagh)
[b]*Department of Environmental Health Engineering, School of Health, Hamadan University of Medical Sciences, Hamadan, Iran,*
Tel. +98 9188373716; emails: kazem_goodyny@yahoo.com, kgoodini@razi.tums.ac.ir
[c]*Department of Environmental Health Engineering, School of Public Health, Iran University of Medical Sciences, Tehran, Iran,*
Tel. +98 9112346428; Fax: +98 2188607939; emails: mshirzadsiboni@yahoo.com, shirzad.m@iums.ac.ir
[d]*Research Center of Health and Environment, Guilan University of Medical Sciences, Rasht, Iran*

ABSTRACT

The Fe$_3$O$_4$–WO$_3$–3-aminopropyltriethoxysilane (APTES) nanoparticles were applied as a heterogeneous catalyst in the presence of UV irradiation for acid red 14 (AR14) removal. This nanocatalyst was synthesized via a facile co-precipitation method and characterized by X-ray diffraction, Fourier transform infrared spectroscopy, scanning electron microscopy, energy dispersive X-ray spectroscopy, vibrating sample magnetometer and point of zero charge techniques. The effects of some operating parameters such as solution pH, nanocatalyst dosage, initial AR14 concentration, H$_2$O$_2$ concentration, different purging gases and type of organic compounds on the removal efficiency were studied. Under optimal conditions: pH = 3, [AR14]$_0$ = 30 mg/L, nanocatalyst dosage = 0.2 g/L and H$_2$O$_2$ = 50 mM, 99.99% of the dye was removed after 120 min. As nanocatalyst dosage increased, the photocatalytic removal of AR14 enhanced up to the desired amount of 0.4 g/L. Moreover, the removal efficiency increased with increasing H$_2$O$_2$ concentration and in the presence of different purging gases. And, the photocatalytic removal of AR14 increased in the presence of oxalate, citric acid, phenol and Ethylenediaminetetraacetic acid, and decreased in the presence of folic acid and humic acid. Three kinetic models were developed for this process and the findings showed that the dye removal rate obeyed the first-order kinetic. Estimation of the E_{EO} value for the UV/Fe$_3$O$_4$–WO$_3$–APTES (288.88 kWh/m^3) process, as a function of the removal efficiency, revealed that this process not only increased the efficiency, but also decreased the cost of electrical energy consumed by the system. Additionally, the photocatalytic activity was maintained even after five successive cycles.

Keywords: Photocatalysis; Acid red 14 removal; Nanocatalyst; Synthesis; UV irradiation

1. Introduction

Many industries such as textile, paper, cosmetic, leather, plastics, food, printing and so on generate a great deal of effluents containing various dyes [1–3]. Treatment of dye-laden wastewaters is very important because dyes may cause aesthetic problems in the environment [4,5]. Besides, application of oxidation, hydrolysis or other chemical measures may result in second by-products, which are by far more dangerous than initial molecules of dyes [4,5]. Acid red 14 (disodium 4-hydroxy-2-[(*E*)-(4-sulfonato-1-naphthyl)diazenyl]naphthalene-1-sulfonate) has the –N=N– functional group in its structure and

* Corresponding author.

is considered as a synthetic red dye [6,7]. This dye is resistant to biological processes and highly toxic and mutagenic [6,7]. Thus, in order to treat well azo dye-based wastewaters, beneficial methods such as adsorption, chemical coagulation, membrane processes, bioremediation, conventional and advanced oxidation processes (AOPs) and photocatalyst are needed [8–10]. In AOPs, hydroxyl radicals with high oxidation power are generated, which can lead to complete decomposition or transformation of contaminants to a less harmful combination [8,11,12]. Some AOPs, which have frequently been utilized for treating various pollutants, are as follows: UV/O_3, UV/H_2O_2, UV/ZnO, UV/TiO_2, $UV/ZnO–TiO_2$ and solar/nanocatalyst processes [8,11–15]. Since photocatalysts have high activities, they have recently been considered to be used in different environmental usages like water and wastewater disinfection [8,11,12,16,17]. So as to make the photocatalytic process more efficient, some procedures like phase and morphological control, doping, surface sensitization and so forth can be applied [18,19]. Interestingly, nanoscaled photocatalysts with a controlled morphology possess enhanced photocatalytic activities due to their high purity, novel morphology and large surface area [18,19]. In order to prepare nanostructured semiconductor photocatalysts having high photocatalytic properties, a few shape-controlled synthesis routes have been used [19]. Great attention has been taken to nanostructured tungsten oxide (WO_3) because it can be applied in many applications like gas sensors, photocatalysts, electrochromic devices, field-emission devices and solar-energy devices [20–24]. One of the main upsides of WO_3 is that it can be separated from aquatic systems by means of filtration and, more importantly, regenerated for further usage [20–24]. But filtration is a time-consuming method resulting in blockage in filters [23]. Magnetic separation is an environmentally benign method because it does not create any pollutants and can treat huge volumes of effluents in short time [25]. Since Fe_3O_4 exhibits superparamagnetic characteristics, this magnetic material can be recovered easily via an external magnetic field and reused without losing the active sites [26,27]. An alternative to conventional adsorbents is the process in which the tungsten oxide nanoparticles are applied in conjunction with Fe_3O_4; in this case, huge amounts of wastewater can be treated [26,27]. However, weak photocatalytic activity is the downside of pure WO_3 as its conduction-band level (0.5 V vs. Normalized Hydrogen Electrode (NHE)) is approximately low [24]. Since the conductivity and conduction band (CB) level (1 V vs. NHE) of Fe_3O_4 are high, which is a suitable option to be coupled with WO_3 and enhances photocatalytic performance through increasing charge transport, we did the current research [24]. Most of the magnetic nanocomposites suffer from some problems like leaching under acidic conditions, being susceptible to autoxidation and toxicity [28,29]. In order to decrease these displeasing properties, the surface of the bare magnetic nanocomposite should be protected [28,29]. Thus, magnetic nanocomposites are embedded in a polymeric, hybrid or inorganic matrix [28,29]. The performance, capacity and selectivity of these materials can be improved when functional groups are on the nanoparticles surface, which can interact with target molecules [28,29]. Cationic and anionic compounds can be removed from aqueous solutions by the amino groups, which are of functional groups. Aminosilane coupling agents can quickly form monolayers on different surfaces; in this case, the surface properties are changed to the modified surfaces by introduction of $–NH_2$ groups [28,29]. An aminosilane has been used for modification of magnetite particles' surfaces for lipase immobilization, wear properties improvement and DNA purification [28,29].

In this study, the removal efficiency of acid red 14 (AR14) using the $Fe_3O_4–WO_3$-3-aminopropyltriethoxysilane (APTES) nanoparticles was investigated. Moreover, the effects of different parameters: solution pH, catalyst dosage, initial AR14 concentration, H_2O_2 concentration, different purging gases and type of organic compounds were studied in the presence of UV irradiation. Also, a kinetic study was conducted and simulated with the zero, first, second and Langmuir–Hinshelwood kinetic models. The electrical energy per order (E_{Eo}) was calculated to evaluate the cost-efficiency of the processes.
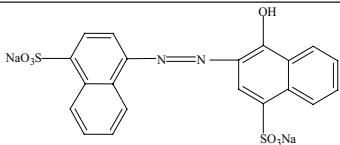
2. Materials and methods

2.1. Chemicals

All chemicals, including tungsten chloride, $FeCl_3.6H_2O$, $FeCl_2.4H_2O$, APTES, sodium hydroxide, folic acid, citric acid, humic acid, oxalic acid, phenol, Ethylenediaminetetraacetic acid (EDTA) and hydrochloric acid, were of analytical grade or of the highest purity available and obtained from Merck (Darmstadt, Germany). It should be noted that the chemicals were used without further purification. AR14 dye was purchased from Alvan Sabet Co., Iran. Table 1 presents a summary of dye properties. A 125 W medium-pressure UVC lamp emitting a maximum wavelength at 247.3 nm was used as the light source. The light intensity of the UVC lamp was 1,020 µW/cm² recorded by a digital radiometer (Model DRC-100X, SPECTROLINE) combined with a DIX-365 radiation sensor (ShokofanTosee, Iran). The photocatalytic reactor used in a previous work was employed for the removal of AR14 [30]. A Metrohm model 713 pH meter was applied for pH measurements and NaOH or HCl (0.1 mol/L) were added to adjust pH values.

2.2. Synthesis of amino-functionalized of $Fe_3O_4–WO_3$ nanoparticles

2.2.1. Synthesis of WO_3 nanoparticles

First, a stock solution (pH 4.83) of 0.1 M tungsten chloride (WCl_6) was prepared by dissolution of WCl_6 into deionized

Table 1
Chemical structure and characteristics of AR14

Color index name	C.I. acid red 14
Chemical structure	
Chemical class	Anionic, azo
Molecular formula	$C_{20}H_{12}Na_2N_2O_7S_2$
Color index number	14720
λ_{max} (nm)	515
Molecular weight (g/mol)	502.43

water [24]. Moreover, an alkaline stock solution (pH 13.8) of 0.6 M sodium hydroxide (NaOH) was prepared by dissolution of NaOH into deionized water. Then, the synthetic reactions were fundamentally carried out by mixing the stock WCl_6 solution, alkali NaOH solution and a certain amount of deionized water (for 7 h). The final pH of the mixture was fixed at 12.5. Next, the obtained product was centrifuged using a centrifuge (Sigma-301, Germany), washed with distilled water for the removal of free WO_3 nanoparticles and then dried at 100°C in an oven for 3 h. Finally, the sample was calcined at 300°C.

2.2.2. Synthesis of Fe_3O_4–WO_3 nanoparticles

First, in alkaline solution, the Fe_3O_4–WO_3 nanoparticles were prepared by means of the co-precipitation and hydrothermal methods [24,25,27]. Next, the appropriate amounts of $FeCl_3.6H_2O$ and $FeCl_2.4H_2O$ were dissolved in 200 mL of deionized water and the WO_3 nanoparticles were added to the suspension at 1:1 volume ratio. After that, 25 mL of NH_4OH (25%) was added dropwise to the precursor solution to achieve an alkaline medium (pH = 8) producing a black and gelatinous precipitate of the Fe_3O_4–WO_3 nanoparticles under nitrogen gas. Then, it was heated at 80°C for 2 h with continuous stirring. Next, the desired catalyst of the Fe_3O_4–WO_3 nanoparticles was collected by a permanent magnet and then washed with deionized water and ethanol for five times. Finally, it was dried at 80°C in a vacuum oven for 5 h.

2.2.3. Synthesis of amino-functionalized Fe_3O_4–WO_3 nanoparticles

The amino-functionalized Fe_3O_4–WO_3 nanoparticles were prepared by means of the co-precipitation and hydrothermal methods. First, the appropriate amount of the Fe_3O_4–WO_3 nanoparticles was dispersed in 400 mL of deionized water. Next, the mixed solutions containing ethanol and APTES were added to the suspension at 1:1 volume ratio at 70°C for 6 h under vigorous stirring. Then, the resulting mixture was washed with deionized water and ethanol for five times. Finally, it was dried at 80°C in a vacuum oven for 5 h [31]. The crystal structure of the samples was determined by X-ray diffraction (XRD) at room temperature using a D8 Advance diffractometer (Bruker, Germany) with monochromatic high-intensity Cu Kα radiation (l = 1.5406 Å), the accelerating voltage of 40 kV and the emission current of 30 mA. The functional groups on the surface of the samples were determined by Fourier transform infrared spectroscopy (FTIR) analysis (Tensor 27, Bruker, Germany), which was in the range of 400–4,000 cm^{-1}. Also, the surface morphology of the samples was determined by scanning electron microscopy (SEM; TESCA MIRA3, Czech Republic). Energy dispersive X-ray spectroscopy (EDX; TESCA MIRA3, Czech Republic) was used to characterize the elemental composition of the samples. And, the magnetic property of the samples was characterized by a vibrating sample magnetometer (VSM; MDKFD, Iran). The point of zero charge (pH$_{zpc}$) was determined to investigate the surface charge properties of catalyst materials. The pH$_{zpc}$ of the samples was measured based on the previously reported method [32].

2.3. Experimental setup

The stock solution (1,000 mg/L) of the dye was prepared by dissolving AR14 into distilled water. The experiments were conducted with different nanocatalyst doses (0.1–0.8 g/L), initial AR14 concentrations (10–100 mg/L), initial pHs (3–11), H_2O_2 concentrations (2–50 mM), oxygen and nitrogen flow rate (2 L/min) and different organic combinations: humic acid, oxalate, EDTA, phenol, folic acid and citric acid (equal to 30 mg/L). All runs were carried out under ambient conditions for 2 h. The batch experiments were performed at (25°C ± 1°C) and continuously stirred. For the photocatalytic removal of AR14, a solution containing a known concentration of AR14 and the nanocatalyst was prepared and allowed to equilibrate for 30 min. At each stage, 10 mL of the suspension was taken at definite time intervals. The nanocatalyst was separated from the mixture solution by permanent magnet for 2 min. The concentration of AR14 in each sample was measured using a spectrophotometer (UV/Vis Spectrophotometer, Hach-DR 5000, USA) at λ_{max} = 515 nm by a calibration curve, which was depicted based on Beer–Lambert law [33].

3. Results and discussion

3.1. Characterization of nanocatalyst

3.1.1. XRD analysis

Fig. 1(a)–(d) show the XRD patterns of the nanoparticles. The crystalline structure of both WO_3 and Fe_3O_4 and Fe_3O_4–WO_3–APTES is exhibited by these patterns even after coating of the Fe_3O_4 nanoparticles onto WO_3. The main peaks at 2θ values of 21.16°, 35.53°, 43.12°, 57.09° and 62.82° corresponded to the (002), (103), (004), (321) and (400) planes of orthorhombic Fe_3O_4 (JCPDS card no. 031156) [27]. And, the main peaks at 2θ values of 23.707°, 24.099°, 26.587°, 28.776°,
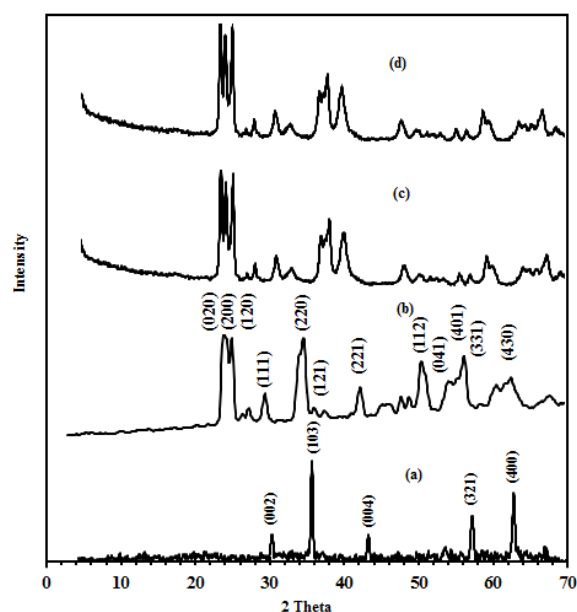

Fig. 1. XRD image of the samples: (a) Fe_3O_4, (b) WO_3, (c) Fe_3O_4–WO_3 and (d) Fe_3O_4–WO_3–APTES.

34.022°, 35.525°, 41.524°, 50.494°, 54.302°, 55.116°, 57.677° and 62.446° corresponded to the (020), (200), (120), (111), (220), (121), (221), (112), (041), (401), (331) and (430) planes of orthorhombic crystalline WO_3 (JCPDS card no. 36-1451) [34]. The peaks related to the nanoparticles of Fe_3O_4 and WO_3 were still observed after the modification with APTES (Fig. 1). This result presents the growth of the Fe_3O_4 nanoparticle crystal on the WO_3 nanoparticles. The Debye–Scherrer's equation was used to calculate the average crystalline size of the WO_3, Fe_3O_4, Fe_3O_4–WO_3 and Fe_3O_4–WO_3–APTES nanoparticles. The mean crystallite size of the nanoparticles: WO_3, Fe_3O_4, Fe_3O_4–WO_3 and Fe_3O_4–WO_3–APTES were estimated to be 23, 8, 19 and 19.3 nm, respectively.

3.1.2. FTIR analysis

The FTIR analysis on the nanoparticles' surface was carried out ranging between 400 and 4,000 cm^{-1} (Fig. 2(a)–(e)). Significant absorption peaks at 447, 580, 860, 1,403, 1,623, 3,378, 3,788 and 3,850 cm^{-1} were observed by the Fe_3O_4 nanoparticles. In addition, the FTIR spectrum of the WO_3 nanoparticles showed significant absorption peaks at 817.40, 1,449.94, 1,639.29, 2,360.37 and 3,398.37 cm^{-1}. Also, the FT–IR spectrum of the Fe_3O_4–WO_3 nanoparticles showed significant absorption peaks at 445.85, 573.99, 813.4, 940.17, 1,395.19, 1,624.45, 2,360.99, 3,385.3 and 3,741.49 cm^{-1}. And, the FTIR spectrum of the Fe_3O_4–WO_3–APTES nanoparticles illustrated significant absorption peaks at 444.19, 577.47, 793.93, 944.77, 1,114.47, 1,221.31, 1,385.18, 1,507.55, 1,629.27, 2,361.09, 3,410.10, 3,741.3 and 3,853.91 cm^{-1}. The two distinct absorption peaks at 580 and 447 cm^{-1} are attributed to the vibration

of Fe^{3+}–O^{2-} and Fe^{2+}–O^{2-}, respectively [25,27]. The peaks from 700 to 900 cm^{-1} are assigned to the aromatic C–H stretching [25,27]. The peak at ~3,400 cm^{-1} belongs to vibration of –OH group [25,27]. For the band observed between 600 and 800 cm^{-1} corresponds to $\nu(W$–O_{inter}–$W)$ and $\nu(W$–O_{intra}–$W)$ [34]. For the WO_3 nanoparticles, the band observed between 2,800 and 3,500 cm^{-1} corresponds to the $\nu(HOH)$ and $\nu(OH)$ [34]. The band seen between 1,600 and 1,650 cm^{-1} corresponds to δ H_2O [34]. The FTIR analysis supported coating of the Fe_3O_4 nanoparticles onto the WO_3 nanoparticles. After amine modified Fe_3O_4–WO_3 nanoparticles with APTES, the new peaks at 1,507.55, 1,385.18, 557.47 and 600–800 cm^{-1} corresponding to N–H, C–N bending vibration, Fe–O vibration of Fe_3O_4 and $\nu(W$–O_{inter}–$W)$ and $\nu(W$–O_{intra}–$W)$ were observed in the spectrum of the Fe_3O_4–WO_3–APTES nanoparticles. These observations provide evidence that amine groups have been successfully introduced onto the surface of the Fe_3O_4–WO_3 nanoparticles, forming the APTES–Fe_3O_4–WO_3 nanocatalyst.

3.1.3. SEM, EDX and VSM

Scanning electronic microscopy (SEM) was used to investigate morphology, shape and size of the Fe_3O_4, WO_3, Fe_3O_4–WO_3 and Fe_3O_4–WO_3–APTES nanoparticles. The SEM images of the Fe_3O_4, WO_3, Fe_3O_4–WO_3 and Fe_3O_4–WO_3–APTES nanoparticles have been shown in Fig. 3(a)–(d), respectively. Fig. 3(a) shows the high-magnification SEM images of the Fe_3O_4 microspheres. It can be seen that the Fe_3O_4 microspheres have a relatively uniform diameter of about 20 nm. Fig. 3(b) shows the morphology of the WO_3 nanoparticles. It can be seen that there is a collection of spherical particles which were agglomerated randomly. Many of the particle size were falling in the range of 10–30 nm, which is in high correlation with the XRD data. Fig. 3(c) presents that the Fe_3O_4-WO_3 precursors are composed of non-uniform sheets with a size range of 10–20 nm. High-magnification SEM shows that large
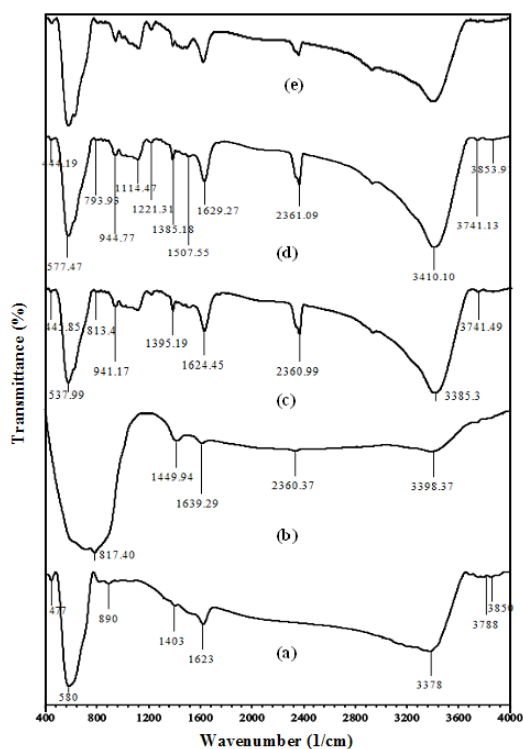

Fig. 2. FTIR image of the samples: (a) Fe_3O_4, (b) WO_3, (c) Fe_3O_4–WO_3, (d) Fe_3O_4–WO_3–APTES and (e) recovery.
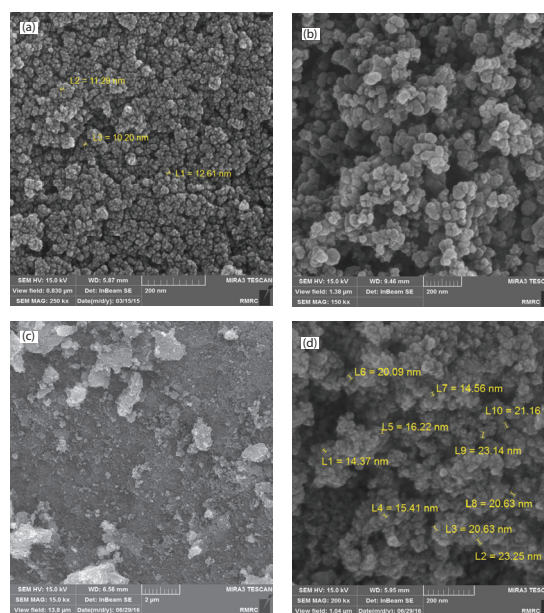
Fig. 3. SEM image of the samples: (a) Fe_3O_4, (b) WO_3, (c) Fe_3O_4–WO_3 and (d) Fe_3O_4–WO_3–APTES.

numbers of the WO_3 nanoparticles have radially grown on the surfaces of the Fe_3O_4 microspheres. Fig. 3(d) clearly illustrates the distribution of APTES on the surface of the Fe_3O_4–WO_3 nanoparticles. Also, Fig. 3(d) shows sphere structure for the Fe_3O_4–WO_3–APTES nanoparticles. The EDX patterns of the Fe_3O_4, Fe_3O_4–WO_3 and Fe_3O_4–WO_3–APTES nanoparticles have been presented in Fig. 4(a). According to the results of the EDX analysis, the weight percentages of C, O and Fe in Fe_3O_4 nanoparticles were 20.94%, 26.07% and 45.28%, respectively; weight percentages of O, Fe and W in Fe_3O_4–WO_3 nanoparticles were 12.53%, 78.29% and 11.68%, respectively; and weight percentages of C, O, Fe and W in Fe_3O_4–WO_3–APTES nanoparticles were 2.06%, 21.19%, 64.29% and 9.98%, respectively. Therefore, the synthesized compound was composed of Fe, O and W, indicating the formation of the Fe_3O_4–WO_3–APTES nanoparticles. VSM magnetization curve of the samples at room temperature has been depicted in Fig. 4(b). The saturated magnetization values were 58.97, 43.83, 42.74 and 0.0043 emu/g, respectively, for the Fe_3O_4, Fe_3O_4–WO_3–APTES, Fe_3O_4–WO_3 and WO_3 nanoparticles.

3.2. Effects of operational parameters on the photocatalytic removal of AR14

3.2.1. Effect of initial pH

Before addition of HCl or NaOH, the pH value of AR14 aqueous solutions was approximately 5.83. The effect of the variable: solution pH on AR14 (30 mg/L) removal via the photocatalytic process was studied by changing initial pH at the constant nanocatalyst dosage (0.2 g/L). An approximate 80%

drop was observed in removal efficiency of AR14 when pH increased from 3 to 11 (Fig. 5). The pH variable played a basic role in the photocatalytic destruction of this compound under the UV/Fe_3O_4–WO_3–APTES process. After the achievement of adsorption equilibrium (30 min), adsorptive removal efficiencies were 30.21, 8.2, 2.3, 1.3 and 0.86% at pH values of 3, 5, 7, 9 and 11, respectively. The removal efficiency at pH of 3 increased to just over 60% after only 15 min of irradiation, but it declined under 3% at pH of 11. The pH_{zpc} was detected for studying the surface charge of the catalyst; the pH_{zpc} values of the nanoparticles: WO_3, Fe_3O_4, Fe_3O_4–WO_3 and Fe_3O_4–WO_3–APTES were found to be, respectively, 5.09, 6, 7.03 and 8.22. The surface of the Fe_3O_4–WO_3–APTES nanoparticles was positively charged at pH values under 8.22, whereas a reverse pattern was seen at values over 8.22. But the repulsion between the negatively charged surfaces of AR14 and the Fe_3O_4–WO_3–APTES nanoparticles declines in acidic conditions [6,8]. Thus, AR14 adsorption onto the nanoparticles of Fe_3O_4–WO_3–APTES goes up, resulting in a better removal efficiency [6,8]. Since there is a sulfuric group in the structure of this compound, and it is negatively charged in acidic solutions, the adsorption of the dye onto the photocatalyst's surface is higher [6,8]. In addition, in acidic conditions, the photocatalytic destruction of the dye happens owing to the formation of •OH (Eqs. (1)–(4)) [12].

$$e_{CB}^- + O_{2(ads)} \rightarrow {}^\bullet O_{2(ads)}^- \tag{1}$$

$$^\bullet O_{2(ads)}^- + H^+ \rightarrow HO_2^\bullet \tag{2}$$

$$2HO_2^\bullet \rightarrow O_2 + H_2O_2 \tag{3}$$

$$H_2O_2 + {}^\bullet O_{2(ads)}^- \rightarrow {}^\bullet OH + OH^- + O_2 \tag{4}$$
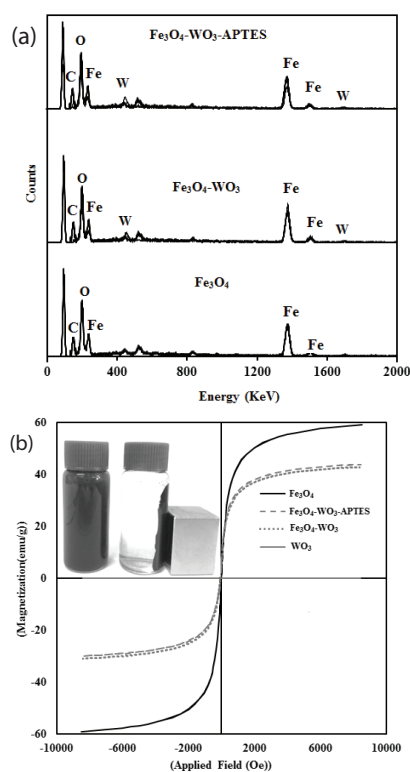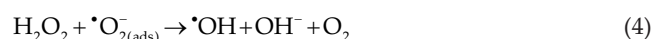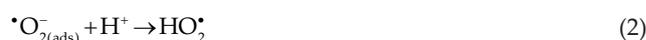

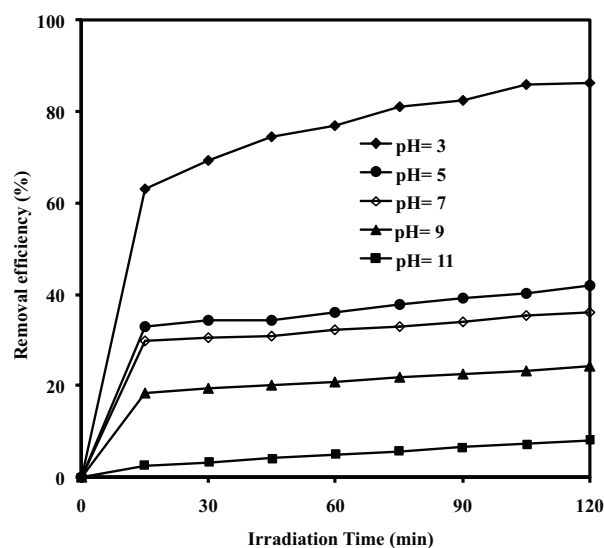Fig. 4. (a) EDX image of the samples and (b) VSM image of the samples.

Fig. 5. The effect of initial pH on the photocatalytic removal of AR14 (catalyst dosage = 0.2 g/L and [AR14]$_0$ = 30 ppm).

It should be pointed that in this study the pH value of 3 was selected as the best value. Therefore, the rest runs were conducted at this value. It was found that this nanocatalyst was stable at pH > 2, based on the pH_{zpc} data.

3.2.2. Effect of catalyst dosage

In this study, it was found that decolorization is dependent on the dosages of the Fe_3O_4–WO_3–APTES nanoparticles. The removal efficiencies of 58.47%, 86.34%, 86.9% and 52.9% were attained at the dosages of 0.1, 0.2, 0.4 and 0.8 g/L, respectively, at AR14 content of 30 mg/L and pH of 3 (Fig. 6). The decolorization went up when there was an increase in the concentration of the catalyst (0.1–0.4 g/L) and then it decreased. It should be noted that the increase of the catalyst amount did not lead to the constant degradation of AR14. The improvement of the removal efficiency can be attributed to: (1) an increase in the content of the Fe_3O_4–WO_3–APTES nanoparticles increasing the number of dye molecules adsorbed on the surface of the catalyst and (2) an increase in the density of catalyst particles in the area of illumination [6,7,35]. The amount of the decolorization declined at dosages above 0.4 g/L of the catalyst, which is because of the aggregation and the reduced activity of the catalyst particles by light scattering [6,7,35]. Other researchers have claimed similar findings [1,11,36]. In the present research, the nanocatalyst dosage of 0.2 g/L was chosen as the optimum amount and other runs were performed at this amount.

3.2.3. Effect of AR14 initial concentrations

Some experiments under the following conditions: six concentrations of AR14 (10, 20, 30, 60, 80 and 100 mg/L), initial pH (3) and constant nanocatalyst dosage (0.2 g/L) were performed to study the effect of initial AR14 concentrations on the efficiency (Fig. 7). As can be seen in Fig. 7, the photocatalytic removal of the dye declined (from 99.99% to 26.33%) when there was an increase in concentration (10–100 mg/L) after 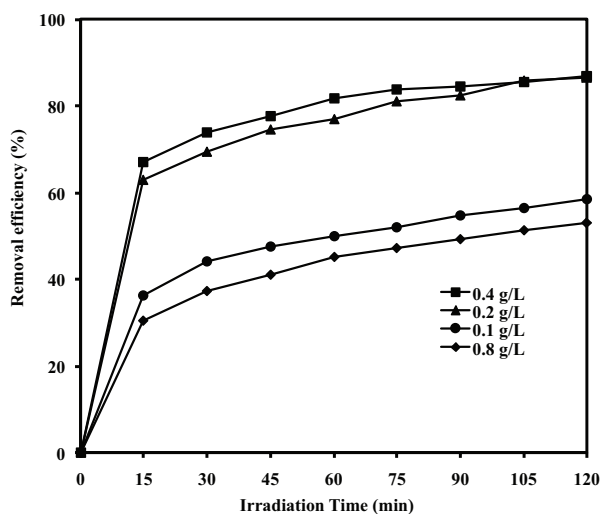120 min. The dye removal performance can be lessened through raising the initial concentration of the dye because in this case more AR14 molecules are absorbed on the surface of the nanocatalyst [8,34,37]. When there is a large amount of adsorbed AR14, the photocatalytic process faces a challenge of an inhibitive impact between AR14 molecules and photogenerated holes or hydroxyl radicals as, in this case, a direct contact does not happen among them [8,34,37]. Furthermore, the path length of photon that enters into the solution declines when the solution contains high contents of AR14 [8,34,37]. Accordingly, other researchers have proven this claim in similar studies [18,38].

3.2.4. Kinetics and electrical energy per order (E_{Eo}) studies

In this part, it was tried to find the appropriate chemical decomposition model, best explaining the experimental kinetic data. Some kinetics models like the zero-, first- and second-order models were used to fit the gained data. It should be pointed that the relationship between initial degradation rate (r) and initial concentration of AR14 can be studied by the Langmuir–Hinshelwood model. Table 2 presents a breakdown of the findings of the equations and constants [23,39,40]. So as to achieve kinetic data for dye removal by the photocatalytic method, $C_0 - C_t$, $\ln[C_0/C_t]$ and $\frac{1}{C_t} - \frac{1}{C_0}$ vs. t were plotted. The zero-, first- and second-order kinetic parameters for photocatalytic models and dye degradation, at different initial contents of AR14 and pH values, have been given in Tables 3 and 4. In the current study, the first-order kinetic model provided a good fit to the data. k_{obs} values for each initial amount (Table 3) were calculated from the slope between $\ln([AR14]_0/[AR14])$ vs. reaction time. The reaction rate of the first-order rate constant (k_{obs}) decreased from 0.0798 to 0.0021 min^{-1} with increasing the concentration of AR14 between 10 and 100 mg/L. E_{Eo} values for six concentrations have been shown in Table 3. With increasing the dye content from 10 to 100 mg/L, the E_{Eo} value increased from 60.15 to 2,285.71 (kWh/m^3). K_{AR14} and k_c were 0.08 (L/mg) and 0.22 (mg/L min) by plotting $1/k_{obs}$ vs. the initial concentration of AR14, respectively. Additionally, the E_{EO} value for the UV/Fe_3O_4–WO_3–APTES (288.88 kWh/m^3) process was

Fig. 6. The effect of catalyst dosage on the photocatalytic removal of AR14 (pH = 3 and $[AR14]_0$ = 30 ppm).

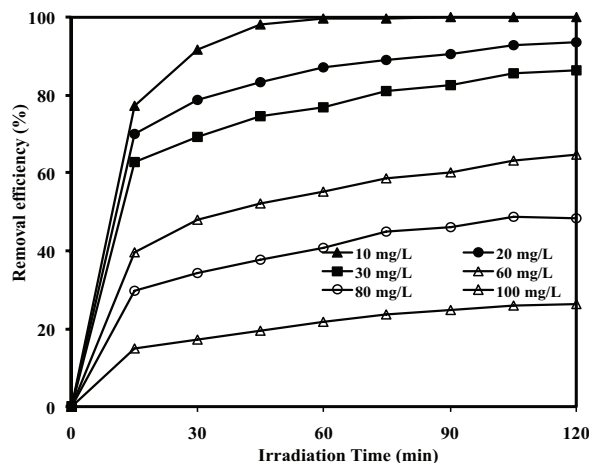
Fig. 7. The effect of initial AR14 concentration on the photocatalytic removal of AR14 (catalyst dosage = 0.2 g/L and pH = 3).

Table 2
Kinetics models, electrical energy per order equations and parameters for the photocatalytic removal of AR14

Kinetic models	Electrical energy per order	Parameters
Zero order $AR14_0 - AP14_t = k_0 t$	$E_{EO} = \dfrac{38.4 \times P}{V \times k_{obs}}$	$AR14_0$ (mg/L), $AR14_t$ (mg/L), k_0 (mol/L)/min, k_{obs} (1/min), k_2 (L/mol)/min, $[AR14]_0$ (mg/L),
First order $\ln \dfrac{AR14_0}{AR14_t} = k_{obs} t$	$E_{EO} = \dfrac{p \times t \times 1000}{V \times 60 \times \log\left(AR14_i \Big/ AR14_f\right)}$	k_c (mg/L)/min, K_{AR14} (L/mg), P (kW), V (L), E_{Eo} (kWh/m^3)
Second order $\dfrac{1}{AR14_t} - \dfrac{1}{AR14_0} = k_2 t$		
Langmuir–Hinshelwood $-\dfrac{d[AR14]}{dt} = \dfrac{k_c K_{AR14}[AR14]}{1 + K_{AR14}[AR14]_0} = k_{obs}\big[AR14\big]$ $\dfrac{1}{k_{obs}} = \dfrac{1}{k_c K_{AR14}} + \dfrac{[AR14]_0}{k_c}$		

Table 3
Kinetic parameters for the photocatalytic removal of AR14 at different initial concentrations of AR14 (catalyst dosage = 0.2 g/L and pH = 3)

$[AR14]_0$ (mg/L)	Zero order		k_{obs} (1/min)	First order		E_{Eo} (kWh/m^3)	Second order	
	k_0 (mol/L)/min	R^2		$1/k_{obs}$ (min)	R^2		k_2 (L/mol)/min	R^2
10	0.054	0.4567	0.0798	12.53	0.9369	60.15	0.5502	0.613
20	0.1053	0.5356	0.0194	51.54	0.8693	247.42	0.006	0.9828
30	0.1489	0.573	0.0136	73.52	0.8303	352.94	0.0016	0.9774
60	0.2402	0.6752	0.007	142.859	0.803	685.71	0.0002	0.9198
80	0.2508	0.7134	0.0046	217.39	0.8004	1,043.48	0.0001	0.6153
100	0.1751	0.7576	0.0021	476.19	0.7965	2,285.71	0.0001	0.8333

Table 4
Kinetic parameters for the photocatalytic removal of AR14 at different initial pHs ($[AR14]_0$ = 30 mg/L and catalyst dosage = 0.2 g/L)

pH	Zero order		First order		Second order	
	k_0 (mol/L/min)	R^2	k_1 (1/min)	R^2	k_2 (L/molmin)	R^2
3	0.1045	0.7431	0.0118	0.9209	0.0016	0.9879
5	0.023	0.9564	0.0012	0.9524	0.0001	0.9479
7	0.0119	0.6003	0.0006	0.6041	0.0001	0.6077
9	0.047	0.0216	0.0003	0.0309	0.0001	0.0416
11	0.0261	0.1412	0.0012	0.1625	0.0001	0.1827

lower than that for the UV/Fe$_3$O$_4$–WO$_3$ (3,242.47 kWh/m^3), UV/Fe$_3$O$_4$ (4,770.72 kWh/m^3), UV/WO$_3$ (2,906.65 kWh/m^3) and UV (2,694.89 kWh/m^3) processes.

3.2.5. Effect of hydrogen peroxide concentration

When the optimum amount of H$_2$O$_2$ was added to the solution, the photocatalytic performance boosted. Of course, the selection of this optimum value is dependent on types and amounts of contaminants. Thus, the performance of the Fe$_3$O$_4$–WO$_3$–APTES nanoparticles in removing AR14 was surveyed under the following conditions: H$_2$O$_2$ concentrations of 2–50 mM, AR14 concentration of 30 mg/L, Fe$_3$O$_4$–WO$_3$–APTES nanoparticles of 0.2 g/L and pH of 3. An increase in initial content of H$_2$O$_2$ (2–50 mM) caused a 15% increase in dye removal (Fig. 8). If H$_2$O$_2$ is added in its

suitable amount, the reaction between H_2O_2 and electron in the conduction band of the Fe_3O_4–WO_3–APTES nanoparticles can be improved. According to Eqs. (5) and (6), H_2O_2 can inhibit the electron–hole recombination [8,41]. Since H_2O_2 can act better as an electron acceptor than O_2, it performs as an alternative electron acceptor to O_2 [8,41]. The removal efficiency is enhanced at high concentrations of H_2O_2 owing to the electron–hole recombination [8,41].

$$H_2O_2 + e_{CB}^- \rightarrow OH^- + HO^\bullet \qquad (5)$$

$$H_2O_2 + h\nu \rightarrow 2HO^\bullet \qquad (6)$$
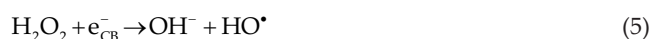
In the study conducted by Daneshvar et al. [11], it was found that addition of H_2O_2 is effective in photodegradation of AR14 by the UV/ZnO process under the conditions as follows: irradiation time of 15 min, $[AR14]_0 = 20$ ppm, ZnO = 160 ppm and pH neutral.

3.2.6. Effect of different purging gases

In the present study, some runs were conducted to determine the effects of different purging gases under the following conditions: oxygen and nitrogen flow rates of 2 L/min, initial AR14 concentration of 30 mg/L, nanocatalyst dosage of 0.2 g/L and pH of 3 (Fig. 9). A higher photocatalyst activity can happen in the situation in which different purging gases are applied, in comparison with the ambient condition. The ambient condition increased the efficiency between 62.89% and 86.34% with increasing time between 15 and 120 min, whereas the removal efficiencies went up from 71.08% to 98.31% and 66.08% to 92.4% in the situation of applying gases: oxygen and nitrogen, respectively. Also, detection of dissolve oxygen (DO) over reaction time illustrated that an increase in time (from 9 to 15 min) caused dissolve oxygen concentration to decrease from 17.36 to 13.02 mg/L (Fig. 9). Generally, it can be concluded that oxygen had the highest removal efficiency followed by nitrogen and without gas
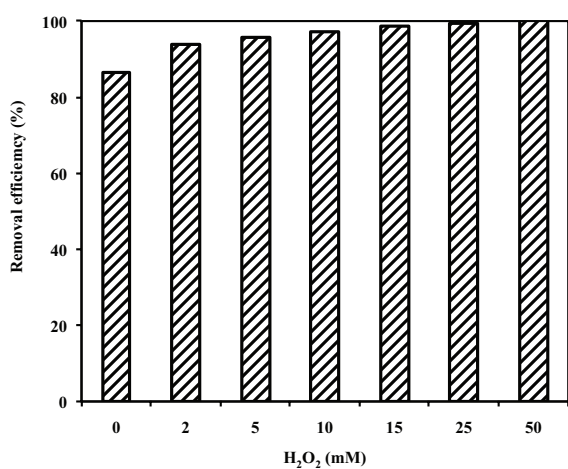
[42]. The photocatalysis stage is dependent on oxygen and nitrogen gases; for example, oxygen is transformed to a superoxide radical anion ($\cdot O_2^-$) by grasping an excited electron in the conduction band of photocatalysts. However, in the case of a situation, in which no gas is employed, the generation of superoxide radicals is limited, thereby providing a less photocatalyst activity for AR14 [42]. In the study by Saharan et al. [43], it was claimed that the removal efficiency of Victoria blue and Fast green FCF enhanced the presence of oxygen gas because of the synergistic effect of Ni doped ZnO nanoparticles and ultrasonication, the efficiency declined by in the case of argon gas. Chakrabarti and Dutta [44] studied photocatalytic destruction of Eosin Y and Methylene Blue dyes by means of ZnO as a photocatalyst; they explained that the efficiency increased between 39% and 63% when the air flow rate was raised between 0 and 11.3 L/min. Pare et al. [45] described that the purging gas of oxygen led to an increase in Lissamine Fast Yellow degradation in ZnO suspension, but the gas of nitrogen declined the efficiency.

3.2.7. Effect of organic compounds

In this research, a few experiments were carried out to measure the impacts of different organic combinations: humic acid, oxalate, EDTA, phenol, folic acid and citric acid (equal to 30 mg/L) under the following conditions: initial AR14 content of 30 mg/L, Fe_3O_4–WO_3–APTES nanoparticles dosage of 0.2 g/L and initial pH of 3. As can be seen in Fig. 10, the proportions of AR14 removal were 98.23, 97.67, 89.39, 89.31, 86.34, 78.31 and 68.23%, respectively, for oxalate, citric acid, phenol, EDTA, without organic compounds, folic acid and humic acid. Organic compounds like citric acid and phenol and EDTA can scavenge the positive holes created over the photocatalytic process, thereby increasing AR14 removal via capturing the promoted electron [32]. On the other hand, folic acid and humic acid declined the performance, which can be on account of the interference between adsorbed organic molecules and AR14 molecules preventing the access of dye molecules to photocatalyst's surface [46]. Also, there are many aliphatic and aromatic organic

Fig. 8. The effect of hydrogen peroxide on the photocatalytic removal of AR14 (catalyst dosage = 0.2 g/L, pH = 3 and $[AR14]_0$ = 30 ppm).
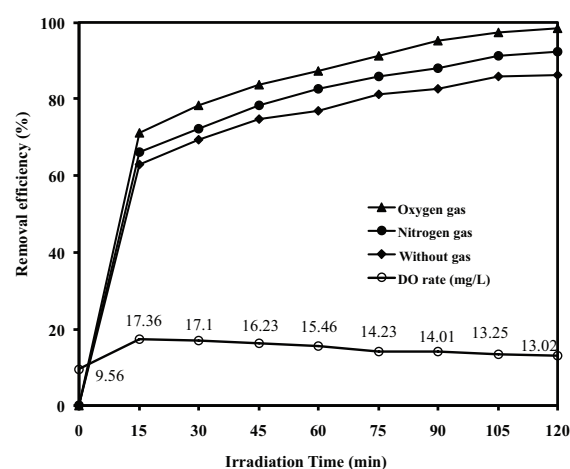
Fig. 9. The effect of different purging gases and variation of dissolved oxygen concentration during the photocatalytic removal of AR14 (catalyst dosage = 0.2 g/L, pH = 3 and $[AR14]_0$ = 30 ppm).

molecules in the structure of folic acid and humic acid [46]. These molecules are subject to the same chemistry as the target analyte and can occupy the photoactive sites on the nanocatalyst's surface; in this case, fewer sites are remained to remove the dye [46]. This competition among molecules would result in a slower removal of the target analyte, AR14 [46]. In the agreement with our results, Chládková et al. [47] explained that the photocatalytic removal of Reactive Red 195 over TiO_2 was reduced in the presence of humic acid, as a scavenging agent.

3.2.8. Comparison of each process

In this research, the performance of different photocatalytic processes: WO_3-alone, Fe_3O_4–WO_3-alone, Fe_3O_4-alone, UV/Fe_3O_4, UV/Fe_3O_4–WO_3, UV/WO_3, UV-alone, Fe_3O_4–WO_3–APTES-alone and UV/Fe_3O_4–WO_3–APTES was evaluated and compared under the same reaction conditions. Initial AR14 concentration, nanoparticle dosage and initial pH were 30 mg/L, 0.2 g/L and 3, respectively. Fig. 11 shows that removal efficiencies for each process were: 8.52, 8.86, 9.63, 11.34, 16.25, 17.94, 19.25, 27.63 and 86.34%, respectively. The photocatalytic removal of AR14 via just adsorption was low. It was found that the UV/Fe_3O_4–WO_3–APTES process had the highest removal efficiency. The photocatalytic removal of this dye by means of the UV/Fe_3O_4–WO_3–APTES process was compared with other reported data. Table 5 shows a breakdown of the efficiencies and kinetics variables for AR14 removal through different methods. The findings illustrated that UV/Fe_3O_4–WO_3–APTES was capable of removing AR14 from aqueous solutions more than UV/Fe_3O_4 and UV/WO_3-alone. In other words, a synergistic effect happens between Fe_3O_4–WO_3 modified with APTES playing an important role in the photocatalytic properties of UV/Fe_3O_4–WO_3-APTES [40].

3.2.9. UV–Vis spectra of AR14 and reusability

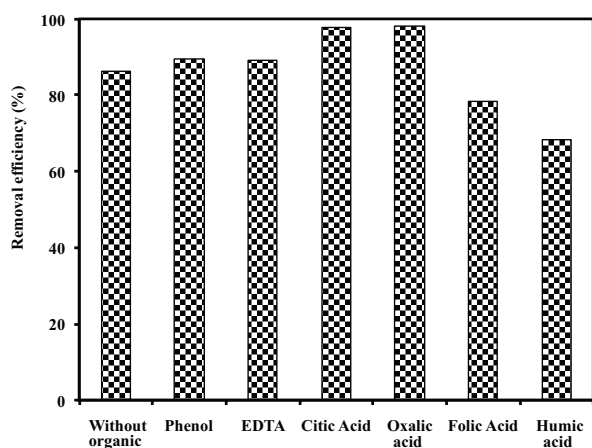The UV–Vis spectra of dye solutions during the photocatalytic process at some irradiation times have been shown in Fig. 12. The spectrum of AR14 in the visible region exhibits a main band with a maximum at 515 nm. As can be seen, a quick decomposition of azo dye occurred because of the fact that the absorption peaks of AR14 at λ_{max} = 515 nm decreased [11]. The decrease is also meaningful with respect to the nitrogen to nitrogen double bond (–N=N–) of the azo dye, as the most active site for oxidative attack [11]. The dye was completely degraded after 2 h under the optimum circumstances.

Because the reusability of a photocatalyst is very important after the reaction, the photocatalyst loaded with contaminant was placed in the 2 M NaOH solution, as a desorbing agent. All photocatalytic experiments were repeated five times in this study. Interestingly, the synthesized photocatalyst had the same photocatalytic activity even after 120 min (Fig. 13).

4. Conclusions

In this study, we synthesized the Fe_3O_4–WO_3–APTES nanoparticles using an easy co-precipitation method; also, the photocatalytic activity of these nanoparticles for AR14 removal was investigated. In order to characterize the produced catalyst, the XRD, FTIR, SEM, EDX, VSM and pH_{zpc} techniques were used. Among all process, UV/Fe_3O_4–WO_3–APTES had the highest photocatalytic activity (at pH 3). The removal efficiency of AR14 increased with raising nanocatalyst dose up to 0.4 g/L and then decreased. An increase in AR14 amount (10–100 mg/L) led to an decrease in reaction rate of the first-order rate constant (k_{obs}) from 0.0798 to 0.0021 min⁻¹. The E_{Eo} value increased between 60.15 and 2,285.71 (kWh/m³) when the concentration of AR14 was raised (10–100 mg/L). And, K_{AR14} and k_c were, respectively, 0.08 (L/mg) and 0.22 (mg/L min). Moreover, a rise in H_2O_2 content in the presence of different purging gases enhanced the performance of the photocatalytic process. Also, the removal efficiency increased in the presence of oxalate, citric acid, phenol and EDTA and declined in the presence of folic

Fig. 10. The effect of different organic compounds on the photocatalytic removal of AR14 (catalyst dosage = 0.2 g/L, pH = 3, [AR14]₀ = 30 ppm and organic compounds = 30 ppm).
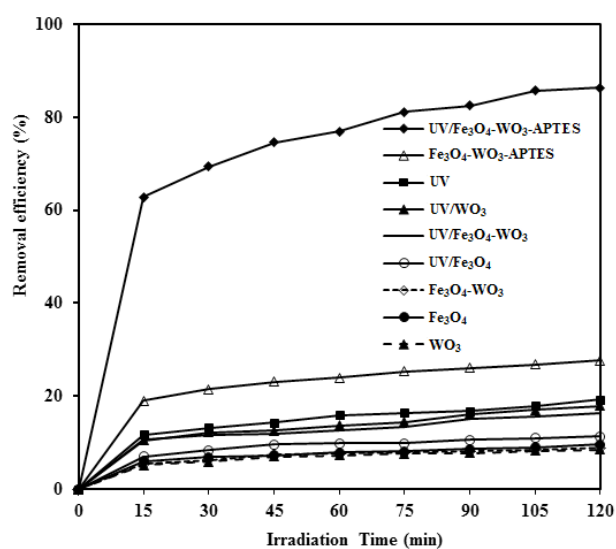

Fig. 11. The contribution of each process involved in the photocatalytic removal of AR14 (catalyst dosage = 0.2 g/L, pH = 3 and [AR14]₀ = 30 ppm).

Table 5
Comparison of the photocatalytic removal of AR14

| Systems	pH	Catalyst dosage (g/L)	$[AR14]_0$ (mg/L)	Lamp (W)	Time (min)	Removal efficiency (%)	L–H parameters K_{AR14} (L/mg)	k_c (mg/L/min)	k_{obs} (min^{-1})	R^2	Reference
UV/GO-CE-TiO$_2$	3	0.04	50	9	120	77.6	–	–	–	–	[6]
Solar Light/TiO$_2$	5.8	0.4	20	7.7 μW/cm^2	60	96.4	–	–	–	–	[35]
UV/ZnO-scallop shell	9	1	30	125	180	100	0.104	0.413	0.0273	0.964	[40]
UV/TiO$_2$	3	0.075	30	15	80	82.1	–	–	0.0341	0.9865	[48]
Visible light/Fe$_3$O$_4$/ZnTi-Layer Doubled Hydroxyl	7	0.05	50	Xenon 500	120	>92	–	–	0.0304	0.9681	[7]
UV/TiO$_2$-glass beads	Natural = 6.7	4 mM	20	30	15	60	–	–	–	–	[18]
Ag/S$_2$O$_8^{2-}$	Natural = 5.8	S$_2$O$_8^{2-}$ = 80 Mm, Ag$^+$ = 0.2 mM	0.04 mM	–	35	80	–	–	–	–	[19]
Fe(II)-Y zeolite/H$_2$O$_2$	5.96	15	50	–	6	Decolorization = 99.3% ± 0.2% Mineralization = 84% ± 5%	–	–	0.9051	0.9964	[9]
UV/Fe-ZSM5/H$_2$O$_2$	5.2	0.25	40	15	20	90	–	–	0.0232	≥0.96	[10]
UV/photoelecro-Fenton-activated carbon fiber cathode	3	1 mM	200	11	360	>94	–	–	–	–	[49]
UV/H$_2$O$_2$/TiO$_2$	Natural = 5.6	–	Dye = 0.1 mM H$_2$O$_2$ = 6 mM	15	50	100	–	–	0.0862	0.9908	[50]
Electro-Fenton-activated carbon fiber cathode	3	1 mM	200	–	360	70	–	–	–	–	[51]
UV/ZnO	Natural	0.16	20	30	60	100	–	–	0.0548	–	[11]
UV/TiO$_2$	Natural	0.04	20	30	210	100	–	–	0.0141	0.9991	[8]
UV/Fe$_3$O$_4$–WO$_3$–APTES	3	0.2	30	125	120	86.34	0.08	0.22	0.0136	0.8303	This study
UV/H$_2$O$_2$/Fe$_3$O$_4$–WO$_3$–APTES	3	0.2	30	125	120	99.99	–	–	–	–	This study
UV/O$_2$/Fe$_3$O$_4$–WO$_3$–APTES	3	0.2	30	125	120	98.31	–	–	–	–	This study
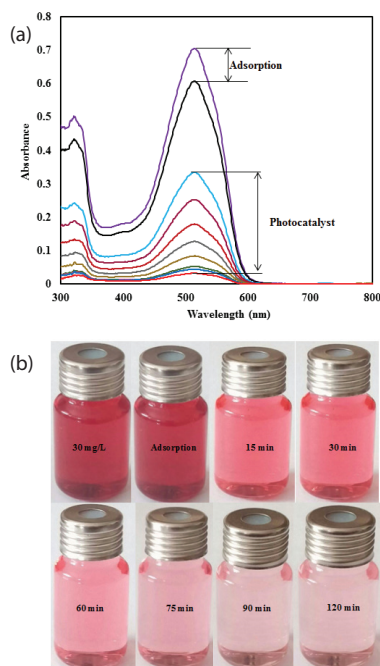
Fig. 12. UV–Vis spectra changes of AR14 in aqueous Fe_3O_4–WO_3–APTES nanoparticle dispersion irradiated with a UV lamp at pH = 3, times: zero, adsorption, photocatalyst (catalyst dosage = 0.2 g/L and $[AR14]_0$ = 30 ppm).

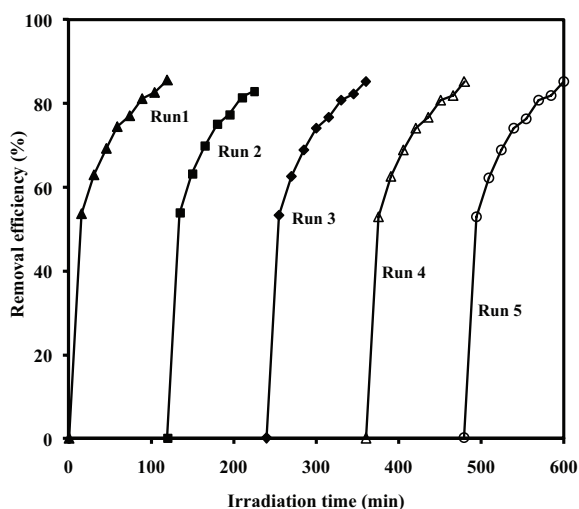Fig. 13. Reusability test for the photocatalytic removal of AR14 within five repeated cycles (catalyst dosage = 0.2 g/L, pH = 3 and $[AR14]_0$ = 30 ppm).

acid and humic acid. Even after five successive cycles, the photocatalytic activity was sustained. The saturation magnetization value of 43.83 emu/g shows that the nanoparticles of Fe_3O_4–WO_3–APTES are simply separated from aqueous solutions through a permanent magnet.

References

[1] A. Aguedach, S. Brosillon, J. Morvan, E.K. Lhadi, Photocatalytic degradation of azo-dyes reactive black 5 and reactive yellow 145 in water over a newly deposited titanium dioxide, Appl. Catal., B, 57 (2005) 55–62.

[2] A. Alinsafi, M. Khemis, M. Pons, J. Leclerc, A. Yaacoubi, A. Benhammou, A. Nejmeddine, Electro-coagulation of reactive textile dyes and textile wastewater, Chem. Eng. Process., 44 (2005) 461–470.

[3] M.N. Chong, Y.J. Cho, P.E. Poh, B. Jin, Evaluation of Titanium dioxide photocatalytic technology for the treatment of reactive Black 5 dye in synthetic and real greywater effluents, J. Cleaner Prod., 89 (2015) 196–202.

[4] Z. Aksu, Biosorption of reactive dyes by dried activated sludge: equilibrium and kinetic modelling, Biochem. Eng. J., 7 (2001) 79–84.

[5] M. Al-Ghouti, M. Khraisheh, S. Allen, M. Ahmad, The removal of dyes from textile wastewater: a study of the physical characteristics and adsorption mechanisms of diatomaceous earth, J. Environ. Manage., 69 (2003) 229–238.

[6] A.G. Akerdi, S.H. Bahrami, M. Arami, E. Pajootan, Photocatalytic discoloration of Acid Red 14 aqueous solution using titania nanoparticles immobilized on graphene oxide fabricated plate, Chemosphere, 159 (2016) 293–299.

[7] S.-j. Xia, X.-b. Zhou, W. Shi, G.-x. Pan, Z.-m. Ni, Photocatalytic property and mechanism studies on acid red 14 by M_xO_y/ZnTi–layered double hydroxides (M = Fe, Sn, Ce), J. Mol. Catal. A: Chem., 392 (2014) 270–277.

[8] N. Daneshvar, D. Salari, A.R. Khataee, Photocatalytic degradation of azo dye acid red 14 in water: investigation of the effect of operational parameters, J. Photochem. Photobiol., A, 157 (2003) 111–116.

[9] R. Idel-aouad, M. Valiente, A. Yaacoubi, B. Tanouti, M. López-Mesas, Rapid decolourization and mineralization of the azo dye C.I. Acid Red 14 by heterogeneous Fenton reaction, J. Hazard. Mater., 186 (2011) 745–750.

[10] M.B. Kasiri, H. Aleboyeh, A. Aleboyeh, Mineralization of C.I. Acid Red 14 azo dye by UV/Fe-ZSM5/H_2O_2 process, Environ. Technol., 31 (2010) 165–173.

[11] N. Daneshvar, D. Salari, A.R. Khataee, Photocatalytic degradation of azo dye acid red 14 in water on ZnO as an alternative catalyst to TiO_2, J. Photochem. Photobiol., A, 162 (2004) 317–322.

[12] N. Daneshvar, A. Khataee, Removal of Azo Dye C.I. Acid Red 14 from Water using Fenton, UV/H_2O_2, UV/H_2O_2/Fe(II), UV/H_2O_2/Fe(III) and UV/H_2O_2/Fe(III)/oxalate processes: a comparative study, J. Environ. Sci. Health, Part. A, 41 (2006) 315–328.

[13] M. Shirzad Siboni, M.-T. Samadi, J.-K. Yang, S.-M. Lee, Photocatalytic removal of Cr(VI) and Ni(II) by UV/TiO_2: kinetic study, Desal. Wat. Treat., 40 (2012) 77–83.

[14] J.K. Yang, S.M. Lee, M. Farrokhi, O. Giahi, M. Shirzad Siboni, Photocatalytic removal of Cr(VI) with illuminated TiO_2, Desal. Wat. Treat., 46 (2012) 375–380.

[15] M. Shirzad-Siboni, A. Jonidi-Jafari, M. Farzadkia, A. Esrafili, M. Gholami, Enhancement of photocatalytic activity of Cu-doped ZnO nanorods for the degradation of an insecticide: kinetics and reaction pathways, J. Environ. Manage., 186 (2017) 1–11.

[16] M. Gholami, M. Shirzad-Siboni, M. Farzadkia, J.-K. Yang, Synthesis, characterization, and application of ZnO/TiO_2 nanocomposite for photocatalysis of a herbicide (Bentazon), Desal. Wat. Treat., 57 (2016) 13632–13644.

[17] M.R. Sammarghandi, J.K. Yang, S.M. Lee, O. Giahi, M. Shirzad-Siboni, Effect of different type of organic compounds on the photocatalytic reduction of Cr(VI) in presence of ZnO nanoparticles, Desal. Wat. Treat., 52 (2014) 1531–1538.

[18] M.H. Rasoulifard, S.M.-M. Doust Mohammadi, A. Heidari, G.H. Shahverdizadeh, Photocatalytic degradation of acid red 14 from contaminated water using immobilized TiO_2 nanoparticles on glass beads activated by UV/peroxydisulfate, Desal. Wat. Treat., 52 (2014) 5479–5484.

[19] M.H. Rasoulifard, S.M.M.D. Mohammadi, A. Heidari, E. Farhangnia, Degradation of acid red 14 by silver ion-catalyzed peroxydisulfate oxidation in an aqueous solution, Turk. J. Eng. Environ. Sci., 36 (2012) 73–80.

[20] T. Arai, M. Yanagida, Y. Konishi, Y. Iwasaki, H. Sugihara, K. Sayama, Efficient complete oxidation of acetaldehyde into CO_2 over $CuBi_2O_4/WO_3$ composite photocatalyst under visible and UV light irradiation, J. Phys. Chem. C, 111 (2007) 7574–7777.

[21] D. Chen, L. Gao, A. Yasumori, K. Kuroda, Y. Sugahara, Size- and shape-controlled conversion of tungstate-based inorganic–organic hybrid belts to WO_3 nanoplates with high specific surface areas, Small, 4 (2008) 1813–1822.

[22] D. Chen, J. Ye, Hierarchical WO_3 hollow shells: dendrite, sphere, dumbbell, and their photocatalytic properties, Adv. Funct. Mater., 18 (2008) 1922–1928.

[23] A. Mohagheghian, S.-A. Karimi, J.-K. Yang, M. Shirzad-Siboni, Photocatalytic degradation of diazinon by illuminated WO_3 nanopowder, Desal. Wat. Treat., 57 (2016) 8262–8269.

[24] G. Xi, B. Yue, J. Cao, J. Ye, Fe_3O_4/WO_3 hierarchical core–shell structure: high-performance and recyclable visible-light photocatalysis, Chem. Eur. J., 17 (2011) 5145–5154.

[25] A. Mohagheghian, R. Vahidi-Kolur, M. Pourmohseni, J.-K. Yang, M. Shirzad-Siboni, Application of scallop shell-Fe_3O_4 nano-composite for the removal azo dye from aqueous solutions, Water Air Soil Pollut., 226 (2015) 1–16.

[26] K. Cheng, S. Peng, C. Xu, S. Sun, Porous hollow Fe_3O_4 nanoparticles for targeted delivery and controlled release of cisplatin, J. Am. Chem. Soc., 131 (2009) 10637–10644.

[27] M. Farrokhi, S.-C. Hosseini, J.-K. Yang, M. Shirzad-Siboni, Application of $ZnO–Fe_3O_4$ nanocomposite on the removal of azo dye from aqueous solutions: kinetics and equilibrium studies, Water Air Soil Pollut., 225 (2014) 1–12.

[28] S.H. Araghi, M.H. Entezari, Amino-functionalized silica magnetite nanoparticles for the simultaneous removal of pollutants from aqueous solution, Appl. Surf. Sci., 333 (2015) 68–77.

[29] T.-g. Yan, L.-j. Wang, Adsorption of C.I. Reactive Red 228 and Congo Red dye from aqueous solution by amino-functionalized Fe_3O_4 particles: kinetics, equilibrium, and thermodynamics, Water Sci. Technol., 69 (2014) 612–621.

[30] M. Shirzad Siboni, M.T. Samadi, J.K. Yang, S.M. Lee, Photocatalytic reduction of Cr(VI) and Ni(II) in aqueous solution by synthesized nanoparticle ZnO under ultraviolet light irradiation: a kinetic study, Environ. Technol., 32 (2011) 1573–1579.

[31] T. Feng, X. Qiao, H. Wang, Z. Sun, C. Hong, A sandwich-type electrochemical immunosensor for carcinoembryonic antigen based on signal amplification strategy of optimized ferrocene functionalized $Fe_3O_4@SiO_2$ as labels, Biosens. Bioelectron., 79 (2016) 48–54.

[32] M. Shirzad-Siboni, M. Farrokhi, R. Darvishi Cheshmeh Soltani, A. Khataee, S. Tajassosi, Photocatalytic reduction of hexavalent chromium over ZnO nanorods immobilized on kaolin, Ind. Eng. Chem. Res., 53 (2014) 1079–1087.

[33] W. Horwitz, Ed., Standard Methods for the Examination of Water and Wastewater, 20th ed., APHA, Washington, D.C., USA, 2000.

[34] A. Mohagheghian, S.-A. Karimi, J.-K. Yang, M. Shirzad-Siboni, Photocatalytic degradation of a textile dye by illuminated tungsten oxide nanopowder, J. Adv. Oxid. Technol., 18 (2015) 61–68.

[35] J. Miao, H.B. Lu, D. Habibi, M.H. Khiadani, L.C. Zhang, Photocatalytic degradation of the azo dye acid red 14 in nanosized TiO_2 suspension under simulated solar light, CLEAN Soil Air Water, 43 (2015) 1037–1043.

[36] P. Bansal, D. Singh, D. Sud, Photocatalytic degradation of azo dye in aqueous TiO_2 suspension: reaction pathway and identification of intermediates products by LC/MS, Sep. Purif. Technol., 72 (2010) 357–365.

[37] A.R. Khataee, M.B. Kasiri, Photocatalytic degradation of organic dyes in the presence of nanostructured titanium dioxide: influence of the chemical structure of dyes, J. Mol. Catal. A: Chem., 328 (2010) 8–26.

[38] J. Rodríguez-Chueca, L.C. Ferreira, J.R. Fernandes, P.B. Tavares, M.S. Lucas, J.A. Peres, Photocatalytic discolouration of Reactive Black 5 by UV-A LEDs and solar radiation, J. Environ. Chem. Eng., 3 (2015) 2948–2956.

[39] A. Jonidi-Jafari, M. Shirzad-Siboni, J.-K. Yang, M. Naimi-Joubani, M. Farrokhi, Photocatalytic degradation of diazinon with illuminated $ZnO–TiO_2$ composite, J. Taiwan Inst. Chem. Eng., 50 (2015) 100–107.

[40] M. Shirzad-Siboni, A. Khataee, B. Vahid, S.W. Joo, S. Fallah, Preparation of a green photocatalyst by immobilization of synthesized ZnO nanosheets on scallop shell for degradation of an azo dye, Curr. Nanosci., 10 (2014) 684–694.

[41] Ö.E. Kartal, M. Erol, H. Oğuz, Photocatalytic destruction of phenol by TiO_2 powders, Chem. Eng. Technol., 24 (2001) 645–649.

[42] M. Gholami, M. Shirzad-Siboni, J.-K. Yang, Application of Ni-doped ZnO rods for the degradation of an azo dye from aqueous solutions, Korean J. Chem. Eng., 33 (2016) 812–822.

[43] P. Saharan, G.R. Chaudhary, S. Lata, S. Mehta, S. Mor, Ultra fast and effective treatment of dyes from water with the synergistic effect of Ni doped ZnO nanoparticles and ultrasonication, Ultrason. Sonochem., 22 (2015) 317–325.

[44] S. Chakrabarti, B.K. Dutta, Photocatalytic degradation of model textile dyes in wastewater using ZnO as semiconductor catalyst, J. Hazard. Mater., 112 (2004) 269–278.

[45] B. Pare, P. Singh, S. Jonnalgadda, Artificial light assisted photocatalytic degradation of lissamine fast yellow dye in ZnO suspension in a slurry batch reactor, Indian J. Chem., Sect. A, 48 (2009) 1364–1369.

[46] W.A. Adams, C.A. Impellitteri, The photocatalysis of *N,N*-diethyl-*m*-toluamide (DEET) using dispersions of Degussa P-25 TiO_2 particles, J. Photochem. Photobiol., A, 202 (2009) 28–32.

[47] B. Chládková, E. Evgenidou, L. Kvítek, A. Panáček, R. Zbořil, P. Kovář, D. Lambropoulou, Adsorption and photocatalysis of nanocrystalline TiO_2 particles for Reactive Red 195 removal: effect of humic acids, anions and scavengers, Environ. Sci. Pollut. Res., 22 (2015) 16514–16524.

[48] A. Bodaghi, R. Moradi, Prediction of photocatalytic decolorization acid red 14 dye in aqueous solutions by UV/NanoTiO$_2$ using artificial neural network model, Int. J. Res. Appl. Sci. Eng. Technol., 2 (2014) 334–340.

[49] A. Wang, J. Qu, H. Liu, J. Ru, Mineralization of an azo dye Acid Red 14 by photoelectro-Fenton process using an activated carbon fiber cathode, Appl. Catal., B, 84 (2008) 393–399.

[50] N.M. Mahmoodi, M. Arami, Bulk phase degradation of Acid Red 14 by nanophotocatalysis using immobilized titanium(IV) oxide nanoparticles, J. Photochem. Photobiol., A, 182 (2006) 60–66.

[51] A. Wang, J. Qu, J. Ru, H. Liu, J. Ge, Mineralization of an azo dye Acid Red 14 by electro-Fenton's reagent using an activated carbon fiber cathode, Dyes. Pigm., 65 (2005) 227–233.